Journal of Nanobiotechnology

RESEARCH Open Access

Injectable celastrol-loading emulsion hydrogel for immunotherapy of low-immunogenic cancer

Yu Liu[1,2†], Jia Zhang[2,3†], Chunyu Lai[2†], Wenjun Wang[4†], Yangyue Huang[5], Xuanwen Bao[2,6], Haimeng Yan[7], Xuqi Sun[2], Qiqi Liu[8], Dong Chen[2,3*], Xiaomeng Dai[2,6,9*], Xinyu Qian[1*] and Peng Zhao[2,6*]

Abstract

Immunotherapy, exemplified by immune checkpoint blockade (ICB), has been extensively employed in antitumor treatments. Nevertheless, its efficacy in addressing low-immunogenic tumors has not yielded satisfactory results, primarily due to the depletion and inadequate infiltration of effector T cells within the tumor microenvironment (TME). Here, we construct an injectable water-in-oil emulsion hydrogel to load clinically used Celastrol (Gel@Cel), which addresses the limitations of Cel's hydrophobicity. Cel can both inhibit tumor cell proliferation and promote tumor cell apoptosis, while simultaneously inducing immunogenic cell death, through activation of the AKT and MAPK pathways. In a model of clinically refractory hepatocellular carcinoma with malignant ascites, intraperitoneal administration of Gel@Cel significantly inhibits tumor progression and activates antitumor immune effects through lipase-controlled release of Cel, as compared to free Cel. Intriguingly, the Gel@Cel induces the activation of dendritic cells, resulting in the infiltration of cytotoxic T cells in the TME of ascites. Furthermore, the administration of Cel increases the expression of programmed cell death protein ligand-1 (PD-L1) in tumor cells. Moreover, combining the PD-1 antibody (αPD-1) with Gel@Cel further enhances the antitumor effect and amplifies the immune activation. In conclusion, Gel@Cel exhibits promising therapeutic potential in the treatment of low-immunogenic tumors, especially when combined with ICB therapy.

Keywords Celastrol, Emulsion hydrogel, Immunogenic cell death, Immune checkpoint blockade

†Yu Liu, Jia Zhang, Chunyu Lai and Wenjun Wang contributed equally to this work.

*Correspondence:
Dong Chen
chen_dong@zju.edu.cn
Xiaomeng Dai
dxm1106@zju.edu.cn
Xinyu Qian
qianxinyu@hospital.westlake.edu.cn
Peng Zhao
zhaop@zju.edu.cn
[1]Department of Medical Oncology, Hangzhou Cancer Hospital, Hangzhou 310002, China
[2]Department of Medical Oncology, The First Affiliated Hospital, School of Medicine, Zhejiang University, #79 Qingchun Road, Hangzhou 310003, China
[3]College of Energy Engineering, State Key Laboratory of Clean Energy Utilization, Zhejiang University, Hangzhou 310027, China
[4]Department of Plastic Surgery, The First Affiliated Hospital, Zhejiang University School of Medicine, Hangzhou 310003, China
[5]Department of Hepatobiliary Pancreatic Oncology, Cancer Center, Integrated Hospital of Traditional Chinese Medicine, Southern Medical University, Guangzhou 510000, China
[6]National Key Laboratory of Advanced Drug Delivery and Release Systems, Zhejiang University, Hangzhou 310058, China
[7]College of Medicine, Bone Marrow Transplantation Center, The First Affiliated Hospital, Zhejiang University, Qingchun Road 79, Hangzhou 310003, China
[8]Department of Radiation Oncology, The First Affiliated Hospital, Zhejiang University, Hangzhou 310003, China
[9]Hubei Key Laboratory of Precision Radiation Oncology, Wuhan 430022, China

Introduction

In recent years, immunotherapy, represented by programmed cell death protein-1 (PD-1)/programmed cell death protein ligand-1 (PD-L1) immune checkpoint blockade (ICB), plays a pivotal role in the treatment of malignant tumors [1, 2]. However, ICB therapy has not demonstrated the expected clinical efficacy in low immunogenic tumors (e.g., hepatocellular carcinoma, malignant ascites, and pancreatic cancer) compared to high immunogenic tumors (e.g., non-small cell lung cancer and melanoma) [3–5]. The principal reason for the ineffectiveness of cancer in responding to ICB therapy is the immunosuppressive tumor microenvironment (TME). The low-immunogenic TME is characterized by the depletion and inadequate infiltration of effector T cells [3, 6]. Hence, it is therefore evident that enhancing T-cell trafficking at the tumor site represents a promising avenue for cancer immunotherapy.

Given that the success of ICB therapy depends critically on the recruitment of effector T cells, a promising therapeutic model is to induce immunogenic cell death (ICD), such as using ICD inducers-oxaliplatin, mitoxantrone, celastrol (Cel) [7]. During the ICD, dying tumor cells release immunostimulatory danger signals, especially calreticulin (CRT), which activates dendritic cells (DCs), resulting in the accumulation of helper T cells and cytotoxic T cells. Cel, a naturally occurring proteasome inhibitor derived from Tripterygium wilfordii, has been demonstrated to possess the potential for remarkable tumor-suppressive efficacy through inhibiting tumor cell proliferation, promoting tumor cell apoptosis, and inducing ICD [8–15]. However, the clinical application of Cel is hindered by its unsatisfactory characteristics, including hydrophobicity, low bioavailability, and systemic toxicity [16]. Hence, it is necessary to develop novel delivery systems for Cel to overcome the afore-mentioned deficiencies in applications while optimizing immune stimulation.

In this work, we constructed an injectable water-in-oil emulsion hydrogel (EHG) to load an ICD inducer-Cel in the continuous oil phase (Gel@Cel). The EHG drug delivery system was developed on the foundation of clinically established iodized oil, with the objective of enhancing its biocompatibility and facilitating its clinical translation. In addition, the EHG system was designed to demonstrate good shear-thinning viscoelastic properties and a high drug-loading capacity, while overcoming the hydrophobicity of Cel. The Gel@Cel demonstrated an exceptional lipase-regulated, sustained release of Cel, which in turn triggers an ICD effect. This subsequently facilitates DC maturation and the priming of effector T cells. Furthermore, considering the elevated PD-L1 expression in tumor cells elicited by Cel, the utilization of anti-PD-1 antibodies (αPD-1) was contemplated as a means of augmenting antitumor immunity in low immunogenic malignant ascites (Fig. 1A). Collectively, our results demonstrated the notable therapeutic efficacy of Gel@Cel-induced ICD and immune activation, offering a promising approach for the management of malignant ascites.

Materials and methods

Reagents

Shellac (wax free) was purchased from Sigma-Aldrich. Iodized oil was acquired from Jiangsu Hengrui Medicine Co., Ltd. Castor oil (USP) was purchased from Aladdin. FITC dextran (MW ~ 10000 Da) and lipase (20000 U/g) were purchased from Macklin. Nile red and phosphate buffered saline (PBS) were purchased from Shanghai Yuanye Bio-Technology Co., Ltd. *α*, *ω*-diamino functionalized polystyrene (NH_2-PS-NH_2, MW ~ 9000 Da) was synthesized *via* atom transfer radical polymerization using a dibromo functionalized initiator and then nucleophilically substituted to yield diamino end groups. Cel was purchased from MCE. Mouse αPD-1 was purchased from Invitrogen. Deionized (DI) water was used throughout the study.

Cell culture

The murine hepatocellular carcinoma cell line H22-luc and Hep1-6, the murine pancreatic cancer cell line KPC were purchased by Shanghai Institute for Biological Science (Shanghai, China) and cultured with Dulbecco's modified Eagle's medium (DMEM, Gibco) containing 10% Fetal Bovine Serum (FBS, Gibco) and 1% penicillin/streptomycin (Meiluncell) in a cellular incubator (37 °C, 5% CO_2).

Preparation of carboxyl functionalized nanoparticles (NPs)

Shellac solution was prepared by dissolving 50 mg shellac in 1 mL of ethanol. Then, 100 μL of the shellac solution was quickly injected into 3 mL of DI water using a 1-200 μL hydrogel-loading pipet tip. Because ethanol quickly mixes with water, shellac precipitates, forming shellac NPs. The particle size was measured using a Zetasizer (Nano series; Malvern). The size distribution of shellac NPs was shown in Figure S1 and the diameter was ~ 120 nm. The shellac NPs contained many carboxyl groups on the surface and were naturally carboxyl functionalized.

Preparation of EHG and Gel@Cel

Emulsion hydrogel (EHG) was prepared. The oil phase consists of iodized oil and castor oil with NH_2-PS-NH_2 at concentration of 10 mg/mL, the water phase contained shellac NPs at concentration of 1.67 mg/mL, and the volume ratio of oil phase to water phase was 1:2. The oil phase and water phase were sheared into water-in-oil

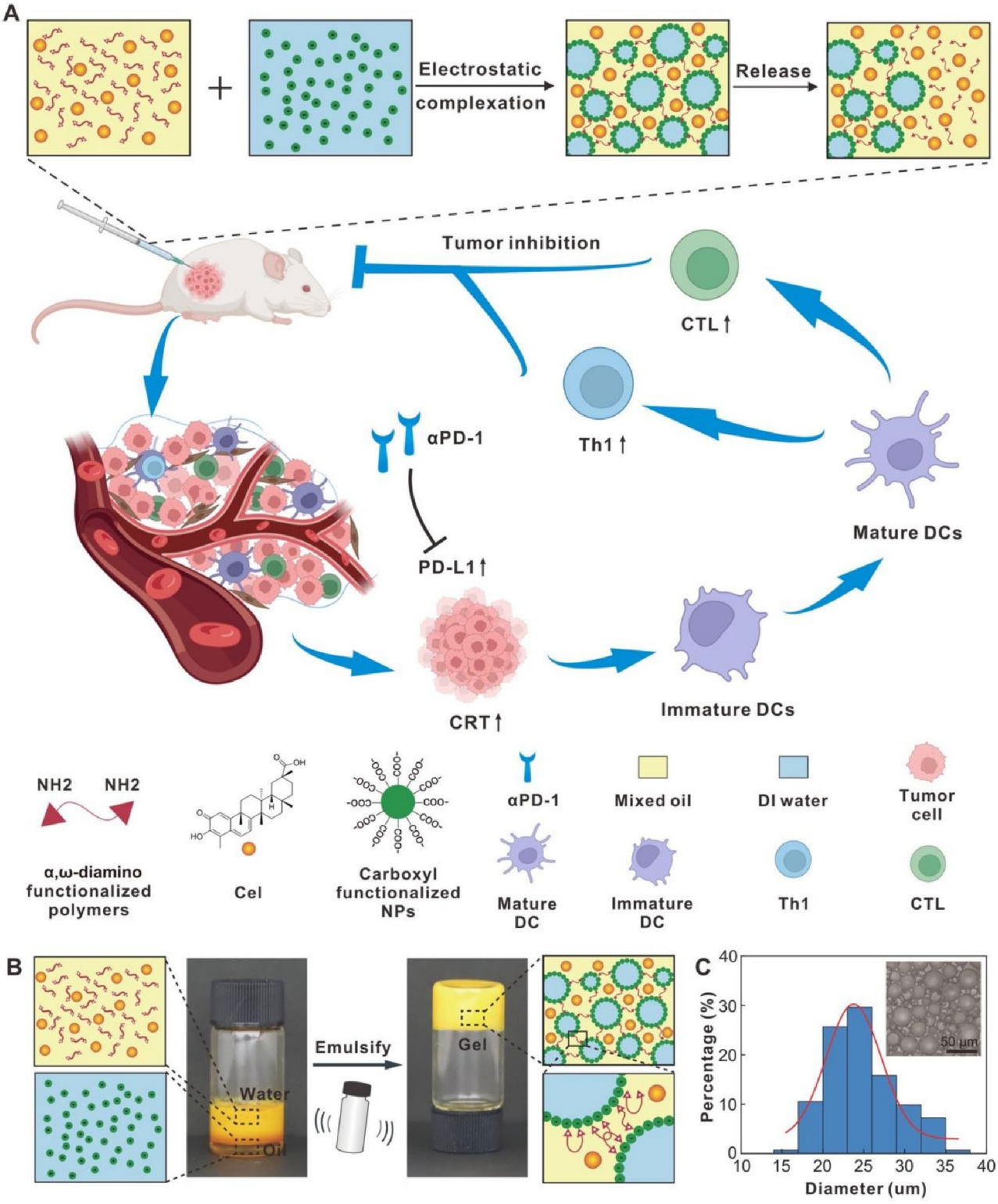

Fig. 1 Construction and preparation of injectable Cel-loading emulsion hydrogel (EHG). **(A)** Schematic representation of the antitumor mechanism of Gel@Cel and αPD-1. **(B)** Preparation of EHG by bridging nanoparticle-stabilized water droplets using telechelic polymers *via* electrostatic complexation. **(C)** Size distribution of EHG at oil to water ratio of 1:2. Inset is the optical microscopic image of water droplets in the oil phase, scale bars represented as 50 μm

emulsions by vortexing, which form EHG after a couple of minutes in stationary. Cel was dissolved in oil phase to prepare Gel@Cel according to the above method. If not specified, the oil phase consists of iodized oil with 20 vol% castor oil.

Confocal Laser Scanning Microscopy (CLSM)

To determine the emulsion type of the EHG systems, Cel in the oil phase as a fluorescent dye. The EHG was imaged using a fluorescent confocal microscope (LSM900, Zeiss) and fluorescence was excited by an Argon laser (405 nm), and red fluorescence emitted by Cel (wavelength 650–800 nm) was detected.

In vitro degradation of EHG

In vitro degradation of EHG at 37 °C was performed by adding 0.45 mL EHG (150 μL oil phase and 300 μL water phase) to the bottom of a 3 mL glass bottle and 1 mL PBS or 1 mL lipase solution (1 mg/mL) on top of the EHG. The oil phases were consisted of iodized oil with different castor oil (5 vol%, 10 vol%, 15 vol% and 20 vol%). To test the release of hydrophilic actives, hydrophilic FITC-dextran was used as the model and loaded in the water droplets. The concentration of FITC-dextran released in the top buffer solution was determined by measuring the absorption peak at 492 nm using a UV-Vis spectrometer (UV-1800, Shimadzu). To test the release of hydrophobic actives, hydrophobic Nile red was used as the model and loaded in the oil phase. The concentration of Nile red released in the top buffer solution was determined by measuring the absorption peak at 550 nm. For every one day, 1 mL top buffer solution was removed for measurement and replaced with 1 mL fresh top buffer solution.

Rheological measurements of EHG

The viscoelastic properties of EHG were measured by a rotating rheometer (MARS 60, HAAKE) equipped with two parallel flat plates (diameter = 20 mm). The EHG used for rheological measurements were prepared using 1.67 mg/mL shellac NPs in water, 10 mg/mL NH_2-PS-NH_2 in the oil phase and different oil-to-water ratio of 1:2. The gap between the two plates was fixed at 1 mm. A solvent-trapping device was placed above the plates to avoid evaporation of the EHG systems. The strain sweeps were conducted from 0.1 to 100% at a constant frequency of 1 rad/s at 25 °C and 37 °C. Frequency sweeps were conducted from 0.1 rad/s to 100 rad/s at a constant strain of 1% at 25 °C and 37 °C. The temperature sweeps were conducted from 20 °C to 50 °C at a constant frequency of 1 rad/s and a constant strain of 1%. The time sweeps were conducted at a constant frequency of 1 rad/s and a constant strain of 1% at 25 °C.

Stability of EHG

The prepared EHG were placed at different temperatures (-20℃, 4℃ and 50℃) for 12 h to test their thermal stability. To test their stability against centrifugation, EHG were centrifuged at different rotational speeds for 5 min.

3D printing of EHG

A 3D printer (Z-603 S, JG AURORA) was modified to simultaneously control the position of the printing head and the infusion of a syringe pump (LSP01-1 A, LongerPump), 2D patterns or 3D models can be printed by EHG. 2D patterns and 3D models were designed and coded into continuous printing paths by a gcode. After the preparation of EHG, the EHG were transferred into a syringe, whose needle was connected to the printing head, and printed into 2D patterns and 3D models. The 3D printing system can simultaneously control the printing paths via the movement of the printing head and the extrusion of EHG along the printing paths via the infusion of the syringe pump. For extrusion-based 3D printing, it was important that the ink could be extruded out of the nozzle and its shape could be maintained after leaving the nozzle. Because of the shearing-thinning viscoelastic property and the water-in-oil emulsion type of the EHG systems, EHG could directly be printed in both air and water.

In vitro cytotoxicity

The cell toxicity of Cel was measured using Cell Counting Kit-8 (CCK-8). H22-luc, Hep1-6, and KPC cells were separately cultured in a 96-well plate for 12 h. Different concentrations of Cel were prepared with 10% FBS-containing DMEM media, and 100 μL solution were added to each culture plate and incubated for 48 h. 10ul CCK-8 assay solution (BS350A, Biosharp) with serum-free DMEM (1:10) was then added to each well and the absorbance at 450 nm was tested after 1 h incubation.

Cell apoptosis detection in vitro

Two groups of H22-luc cells, Hep1-6 cells, and KPC cells were separately planted in six-well plates, and after 12 h, the old DMEM medium was removed, and cells were incubated with PBS, Gel, Cel, or Gel@Cel for 48 h in H22-luc cells and with PBS or Cel for 48 h in Hep1-6 cells and KPC cells. Finally, the cells were collected and incubated with Annexin V-fluorescein isothiocyanate (FITC)/propidium iodide (PI) (AT101, Multi sciences) for 15 min and detected immediately by flow cytometry (FCM, BD Fortessa X-20).

CRT expression in vitro

H22-luc cells, Hep1-6 cells, or KPC cells were separately seeded in six-well plates and incubated with PBS or Cel for 48 h. After different treatments, the cells were

stained with CRT primary antibody (A00894, Boster, 1:50, diluted in PBS) for 30 min, followed by incubation with donkey anti-rabbit IgG (Clone poly4064, Biolegend, 1:200, diluted in PBS) for 30 min. Then, cells were rinsed and resuspended with 100ul PBS, analyzed using a flow cytometer (BD Fortessa X-20).

PD-L1 expression in vitro

To assess PD-L1 expression by flow cytometry, H22-luc, Hep1-6, or KPC cells were separately cultured in six-well plates overnight and then incubated with PBS, Gel, Cel, or Gel@Cel for 48 h in H22-luc cells and with PBS or Cel for 48 h in Hep1-6 cells and KPC cells. Cells were labeled with fluorescent dye-labeled antibodies against PD-L1 (Clone 10 F.9G2, Biolegend, 1:200, diluted in PBS) for 30 min. Finally, the cells were collected and analyzed by flow cytometry (BD Fortessa X-20).

RNA-seq analysis

KPC cells were treated with PBS or Cel. After 24 h, total RNA was extracted using Trizol according to the manufacturer's instructions. RNA-seq was performed by OE Biotech Co., Ltd. (Shanghai, China).

Western blot assay

KPC cells were seeded on 6-well plates overnight, and then were treated with Cel for 0 h, 0.5 h, 2 h, 4 h, respectively. Total proteins were extracted from treated KPC cells. Each protein sample was resolved by SDS-PAGE gel electrophoresis, and then transferred to PVDF membranes (ISEQ00010, Millipore). After incubating with BSA blocking buffer for 1 h, the primary antibodies of p-P38 (4511T, CST, 1:1000), p-JNK (BM4380, Boster, 1:1000), p-ERK (BM4156, Boster, 1:1000), p-AKT (4060T, CST, 1:1000), and β-actin were applied to these membranes overnight at 4 °C. Subsequently, membranes were incubated with horseradish peroxidase-conjugated secondary antibodies for 1 h. Finally, immunoreactive bands of each group were observed by ECL western blotting detection system. The relative protein expression level was quantified using Image J V2 software.

Animal experiment

We purchased BALB/c mice (6 or 7 weeks old) from the Zhejiang of Laboratory Animals (ZJCLA). Mice were housed in a specific pathogen-free facility. All experimental protocols were approved by the Animal Experimental Ethical Inspection of the Institutional Animal Care and Use Committee (IACUC) and ZJCLA with the approval number ZJCLA-IACUC-20,010,637. We constructed a H22-luc hepatocarcinoma ascites model by implanting intraperitoneally 2×10^5 H22-luc cells into BALB/c mice. After six days, tumor-bearing mice were randomly divided into six groups and intraperitoneally treated with 50ul PBS, Cel, Gel, αPD-1, Gel@Cel, or Gel@Cel + αPD-1 (Cel, 5 mg/kg; PD-1,10 mg/kg) every four days for two times. Tumor weights were measured at day 8/11/14. Tumor burden was observed by continuous bioluminescence imaging.

Flow cytometry

Ascites fluid was collected, prepared and labeled with related dyes and antibodies. Zombie NIR™ Fixable Viability Kit (423105; 1:2000) was used to label dead cells. Related antibodies containing CD45-AF700 (Clone 30-F11; 123114), CD86-PE (Clone A17199A; 159204), CD11c-BV510 (Clone N418; 117338), CD45-FITC (Clone QA17A26; 157608), CD3-BV605 (Clone 145-2C11; 100351), CD4-PE (Clone GK1.5; 100408), CD8-BV421 (Clone 53 – 6.7; 100738), and IFN-γ-PE-Cy7 (Clone XMG1.2; 505826) were obtained from Biolegend and diluted with PBS containing 2%FBS or permeabilization buffer at 1:600 ratio. Flow cytometry analyses were performed on a BD Fortessa X-20 flow cytometer.

Quantitative and statistical analyses

All data are presented in figures as means ± SEM. Statistical analyses were performed using GraphPad Prism 10.0 software. The flow cytometry data were analyzed by FlowJo V10 software (TreeStar). Unpaired two-tailed Student's t test was used to compare the difference between two groups of measurements. One-way analysis of variance (ANOVA) was used for comparing two groups in multi-group comparisons. Significant differences are expressed as follows: ns: not significant, $^{*}p < 0.05$, $^{**}p < 0.01$, and $^{***}p < 0.001$.

Results

Preparation and characterization of EHG

In this study, the oil phase and water phase were sheared into water-in-oil emulsions by vortexing, which form EHG after a couple of minutes in stationary. As the carboxyl groups of shellac NPs were negatively charged [17, 18] and the amino end groups of NH_2-PS-NH_2 polymers were positively charged, during the emulsification process, one amino end group can electrostatically bind to one carboxyl group and each NH_2-PS-NH_2 molecule with two amino end groups can simultaneously bind to two shellac NPs in two neighboring droplets, thus performing as a chelator to form emulsion hydrogels. The shellac NPs was essential for the formation of EHG, in the absence of shellac NPs in the water phase, no EHG could be formed, as shown in Figure S2. Hydrophobic Cel can be dissolved in the oil phase, shellac nanoparticles in the water phase, EHG was designed and prepared by emulsifying the water phase into droplets in the continuous oil phase, as shown in Fig. 1B. This approach facilitated the encapsulation of hydrophobic Cel in EHG and its subsequent delivery. The

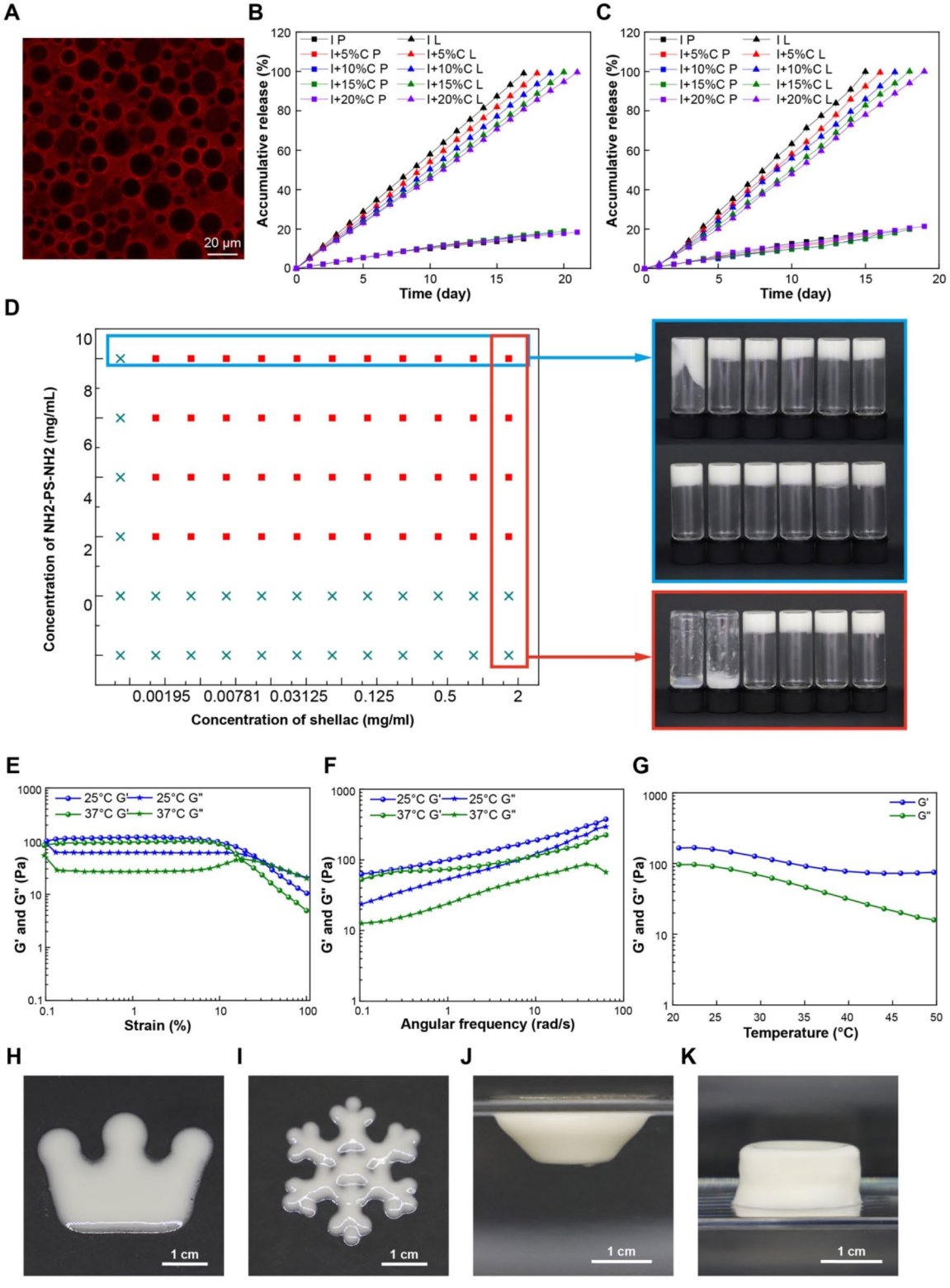

Fig. 2 (See legend on next page.)

(See figure on previous page.)

Fig. 2 Preparation and characterizations of EHG. **(A)** Fluorescent confocal microscopic images of EHG loaded with Cel in oil phase, scale bar represented as 20 μm. **(B)** Release profiles of FITC dextran-loaded droplets of EHG in the presence of PBS (square) and lipase (upper triangle), the EHG are prepared with different oil phase, the oil phase consists of iodized oil (I) with different 0 vol%, 5 vol%, 10 vol%, 15 vol% and 20 vol% castor oil (C). **(C)** Release profiles of Nile red-loaded in the oil phase of EHG in the presence of PBS (square) and lipase (upper triangle), the EHG are prepared with different oil phase, the oil phase consists of a mixture of iodized oil (I) and 0 vol%, 5 vol%, 10 vol%, 15 vol% and 20 vol% castor oil (C). **(D)** Phase diagram of EHG prepared at oil to water ratio of 1:2, with different concentrations of shellac-NPs in water phase and NH_2-PS-NH_2 telechelic polymers in oil phase. If not specified, the oil phase consists of a mixture of 80 vol% iodized oil and 20 vol% castor oil, and the NH_2-PS-NH_2 concentration in the oil phase is 10 mg/mL and the concentration of shellac NPs in the water phase is 1.67 mg/mL. **(E)** Strain sweeps of elastic modulus G′ and viscous modulus G″ at oil to water ratio of 1:2, showing characteristic shear-thinning behaviors. The frequency is held constant at 1 rad/s. **(F)** Frequency sweeps of elastic modulus G′ and viscous modulus G″ at oil to water ratio of 1:2, showing characteristic shear-thinning behaviors. The strain is held constant at 1%. **(G)** Temperature sweeps of elastic modulus G′ and viscous modulus G″ at oil to water ratio of 1:2 from 20 to 50℃. The strain is held constant at 1% and the frequency is held constant at 1 rad/s. **(H-J)** 3D printing of EHG in air. **(K)** 3D printing of EHG directly in water. Scale bars in H, I, J and K are 1 cm

droplets and size distribution of EHG prepared at oil to water ratio of 1:2 was shown in the Fig. 1C, the diameter of droplet is 25 μm. Cel itself was red and has fluorescent, which can be used as a fluorescent indicator in oil phase, as shown in Figure S3, it indicated that Cel was successfully loaded into the EHG. Fluorescent confocal microscopy imaging indicated successfully loading of hydrophobic therapeutics (Fig. 2A and S3), and the EHG was water-in-oil type. To observe the microstructure of EHG more directly, 3D reconstruction showing the EHG from z-scans of fluorescent confocal microscope images in Figure S4, from which dispersed spherical droplets can be seen. By adding a certain proportion of castor oil to the iodized oil, EHG can also be formed. To obtain better slow-release effect, five different EHG with different castor oil (0 vol%, 5 vol%, 10 vol%, 15 vol% and 20 vol% castor oil) in oil phase were prepared and their release properties were tested. Release profiles of FITC-dextran and Nile Red in the presence of PBS (square) and lipase (upper triangle) were shown in Fig. 2B and C, FITC-dextran and Nile Red can be released at the trigger of lipase at a linearly increasing and almost no release in PBS solution. The release of EHG was trigged by lipase, which can gradually decompose the continuous oil phase, thus releasing the encapsulated cargo in a sustained manner. The higher the proportion of castor oil in the oil phase, the slower the degradation of the gel in the lipase. The EHG showed slow release in 20 days when the castor oil was 20 vol% in oil phase, which showed the EHG systems can realize the control and slow release. To successfully prepare EHG, a minimum concentration of shellac-NPs (0.0016 mg/mL) and a minimum concentration of NH_2-PS-NH_2 telechelic polymers (4 mg/mL) were required to ensure gelation (Fig. 2D).

EHG used for the test were prepared of oil phase consisting of a mixture of 80 vol% iodized oil and 20 vol% castor oil, which showed excellent viscoelastic properties. The strain sweeps of EHG prepared at oil to water ratio of 1:2 at different temperatures was shown in Fig. 2E. When the strain was less than 10%, the elastic modulus G′ was larger than the viscous modulus G″ with little change, showing the EHG systems of a non-flowable characteristics. The yield point of strain ≈ 29% and 17% at 25℃ and 37℃, respectively. When the strain larger than yield point, the viscous modulus G″ became larger than the elastic modulus G′ and the EHG became flowable, which was a characteristic shear-thinning behavior. The elastic modulus G′ and the viscous modulus G″ of EHG with angular frequency at 25℃ and 37℃ were shown in Fig. 2F, G′ and G″ increased with increasing angular frequency. The elastic modulus G′ of EHG was greater than viscous modulus G′′ at angular frequency, showing a solid-like characteristics. In addition, the elastic modulus G′ and the viscous modulus G″ of EHG was hardly compromised over 1800s (Figure S5), suggesting the stability of the EHG. The elastic modulus G′ and the viscous modulus G″ decreased with the increase of temperature, which shown in Fig. 2G.

EHG was stable from 4℃ to 50℃, when the temperature below freezing point (e.g., -20℃), the structure of EHG was destroyed due to the crystallization of water. However, stable EHG can be retrieved at room temperature by vortexing (Figure S6). The EHG was also stable against centrifugation speed less than 1000 rpm, when the centrifugation above 1500 rpm, a small amount of oil may release out by compressing the water droplets (Figure S7). The EHG with shear-thinning viscoelastic properties and excellent stability, which can be an ideal ink for 3D printing and can directly print patterns in air, as shown in Fig. 2H, I and J. As the EHG was water-in-oil type, so the EHG can print in water directly, as shown in Fig. 2K.

In vitro antitumor efficacy

To ascertain the antitumor efficacy of Cel in low-immunogenic tumor cells, CCK-8 assays were employed to ascertain the cytotoxicity of Cel in H22-luc cells, Hep1-6 cells and KPC cells. As shown in Fig. 3A and Figure S8, Cel exhibited similar potent toxicity to the above tumor cells in a dose-dependent manner. The half maximal inhibitory concentration (IC50) value of Cel was determined as 0.61 μg/mL, 0.75 μg/mL, and 1 μg/mL in H22-luc cells, Hep1-6 cells and KPC cells, respectively. Cell apoptosis was further evaluated by flow cytometry.

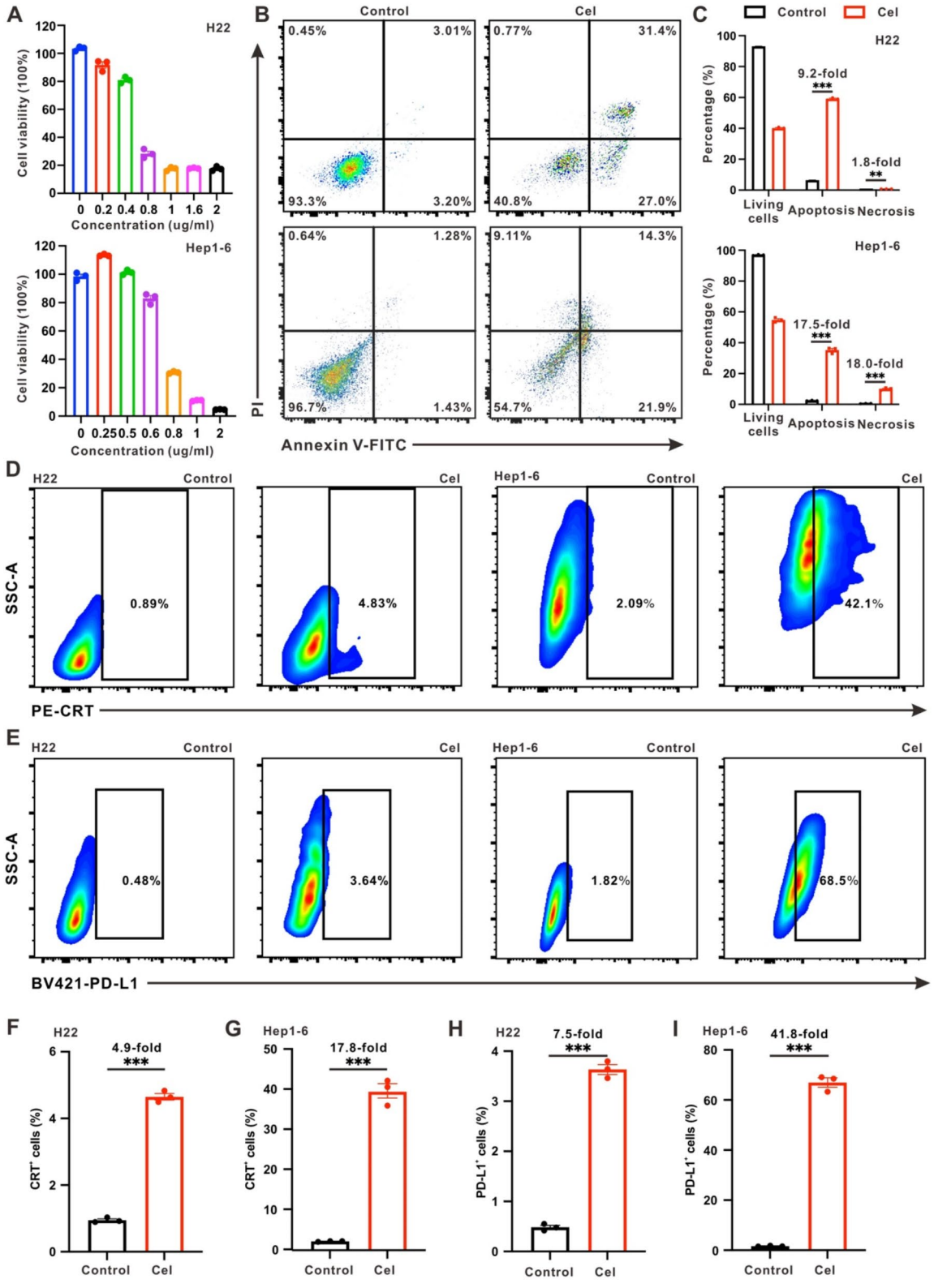

Fig. 3 (See legend on next page.)

(See figure on previous page.)

Fig. 3 Cytotoxicity and inducing immune activation of Cel in vitro. **(A)** Cell viability of H22-luc cells and Hep1-6 cells examined post 48 h incubation with different concentrations Cel. **(B)** Flow cytometry and **(C)** quantitative apoptotic cell analysis of H22-luc cells and Hep1-6 cells after treatment with PBS or Cel. **(D)** Expression of CRT was detected by flow cytometry and **(F, G)** corresponding quantification in H22-luc cells and Hep1-6 cells. **(E)** PD-L1 expression was detected by flow cytometry and **(H, I)** corresponding quantification in H22-luc cells and Hep1-6 cells. Statistical significance was calculated via t-test. Data represent means ± S.E.M. *$p < 0.05$, **$p < 0.01$, and ***$p < 0.001$

Consistent with CCK-8 results, Cel possessed the ability to significantly inhibit the proliferation of tumor cells, in which the killing of tumor cells mainly relies on apoptosis. In Hep1-6 cells and KPC cells, Cel induced 36.2% and 31.7% apoptosis ratios (including early and late apoptosis states), respectively, which were 17.5-fold, and 8.3-fold increases compared with the control group (Fig. 3B-C and Figure S9). To further demonstrate that Gel@Cel has a therapeutic effect comparable to that of Cel, we included Gel and Gel@Cel treatment groups to assess cell apoptosis in H22-luc cells. As shown in Fig. 3B-C and Figure S10, both Cel and Gel@Cel induced tumor cell death via apoptosis, with apoptosis rates increasing 9.2-fold and 10.6-fold, respectively, compared to the control group. This highlighted the effective therapeutic impact of Cel in the Gel state. Meanwhile, H22-luc cells treated with Gel alone showed no significant difference in apoptosis, indicating that the ability of Gel@Cel to induce apoptosis in H22-luc cells was primarily attributed to Cel. Collectively, the afore-mentioned data indicated that Cel exhibited a robust direct tumor-killing effect.

In vitro immune activation effect

Cel as a natural product isolated from Tripterygium wilfordii has considered to provoke antitumor immunity responses by inducing ICD, which is typical of CRT exposure on the dying tumor cells surface [19]. Flow cytometry was performed to verify CRT expression in H22-luc cells, Hep1-6 cells and KPC cells. As shown in Fig. 3D, F-G and Figure S11, when the three cell lines mentioned above treated with appropriate concentrations of Cel (0.8 μg/mL, 0.8 μg/mL, and 1.4 μg/mL), the percentage of CRT-positive cells increased 4.9-fold, 17.8-fold, and 1.7-fold, respectively, compared with control groups. Therefore, the results demonstrated that Cel possessed the capacity to induce a substantial degree of CRT exposure in tumor cells.

Previous studies have demonstrated that ICD inducers are capable of upregulating PD-L1 expression in tumor cells [20, 21]. Hence, we detected the expression of PD-L1 in H22-luc cells, Hep1-6 cells and KPC cells. As illustrated in Fig. 3E and I, compared with PBS group, the expression of PD-L1 increased by 41.8-fold in Hep1-6 cells after Cel treatment, respectively. Similar results were also demonstrated in KPC cells (Figure S12). In addition, as shown in Fig. 3E and H and Figure S13, the percentage of PD-L1 positive cells increased by 7.5-fold and 10.2-fold, compared with control groups. Thus, these results indicated that Cel and Gel@Cel had the capacity to upregulate the expression of PD-L1 in tumor cells, while PD-L1 needed to be blocked to achieve significant antitumor immunotherapeutic effects.

RNA-sequencing analysis

To explore the potential molecular mechanism of antitumor efficacy induced by Cel, RNA-sequencing of KPC cells was performed that were either treated with PBS or Cel. As illustrated in Figs. 4A and 15,837 genes were detected, of which 428 genes were down-regulated and 989 genes were up-regulated in KPC cells treated with Cel, compared with the control group. Subsequently, we observed that some differentially expressed genes (DEGs) were up-regulated expression in the Cel group, including *Fos*, *Ikbkg*, *Gadd45a*, *Gadd45b*, *Gadd45g*, which indicated Cel caused intense cell apoptosis. Furthermore, the elevated mRNA levels of *Hspa1a* indicated the potential for Cel to induce ICD (Fig. 4B). To further access the underlying signaling pathways, Kyoto Encyclopedia of Genes and Genomes (KEGG) enrichment analysis was performed on the DEGs. KEGG analysis elucidated that a variety of antitumor related signaling pathways were changed in KPC cells after Cel treatment, such as TNF signaling pathway, NF-Kappa B signaling pathway, apoptosis, PI3K-AKT signaling pathway, and MAPK signaling pathway (Fig. 4C). Synchronously, Gene Ontology (GO) enrichment analysis of the DEGs revealed Cel-regulated pathways including apoptosis, programmed cell death and MAPK signaling pathway (Figure S14). Considering the correlation of cell apoptosis and ICD with PI3K-AKT and MAPK signaling pathway [22], we further verified the gene sets overall expression trends of the above signaling pathway by Gene Set Enrichment Analysis (GSEA). As shown in Figure S15, compared with the control group, GSEA revealed that the PI3K-AKT and MAPK signaling pathway genes were highly enriched in KPC cells treated with Cel and the above two signaling pathway were up-regulated. We further evaluated the phosphorylation levels of p-AKT protein of the PI3K-AKT pathway, as well as p-P38, p-JNK, and p-ERK proteins of the MAPK pathway using western blotting. Cel treatment with different time (0 h, 0.5 h, 2 h, 4 h) significantly up-regulated p-P38, p-JNK, p-ERK, and p-AKT protein in KPC cells, particularly after 0.5 h of Cel incubation (Fig. 4D, Figure S16). These findings suggested that Cel promoted tumor cell apoptosis and induced ICD via the activation of PI3K-AKT and the MAPK signaling pathway.

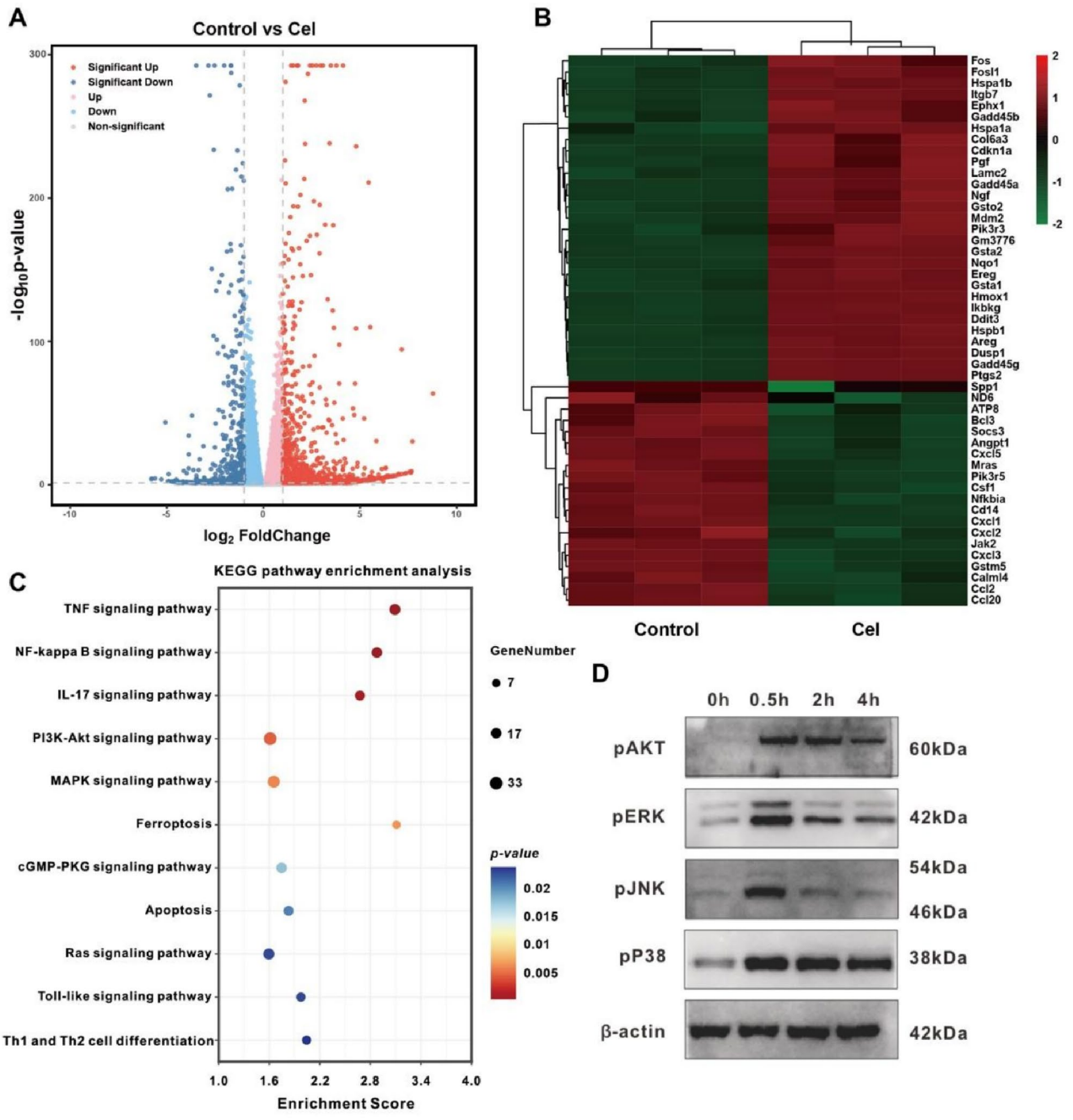

Fig. 4 Genome-wide RNA-sequencing of KPC cells treated with Cel in vitro. **(A)** Volcano plots of the total differentially expressed genes (DEGs) between Cel-treated group and PBS group. **(B)** Heat map of the specific DEGs. **(C)** Kyoto Encyclopedia of Genes and Genomes (KEGG) pathway enrichment analysis. **(D)** The expression levels of p-AKT, p-ERK, p-JNK, and p-P38 were detected in KPC cells treated with Cel at the 0 h, 0.5 h, 2 h, and 4 h by western blotting

In vivo antitumor effects

A luciferase-tagged H22 cells (H22-luc) tumor-bearing BALB/c malignant ascites mouse model was established to evaluate the therapeutic potential of Gel@Cel. We verified the formation of H22-luc hepatoma ascites mice model using bioluminescence imaging and then the mice were randomly divided into five groups to receive various treatments (PBS, Cel, Gel, αPD-1, Gel@Cel, or Gel@Cel + αPD-1). Details of the treatment outline were shown in Fig. 5A. Furthermore, bioluminescence signals of H22-luc cells were monitored for purpose of tracking the progression of malignant ascites. Different treatment groups (Cel, Gel@Cel, and Gel@Cel + αPD-1) possessed the ability of retarding tumor growth to varying degrees in contrast to the control group. Overall, Gel@Cel + αPD-1 caused the highest degree of delaying

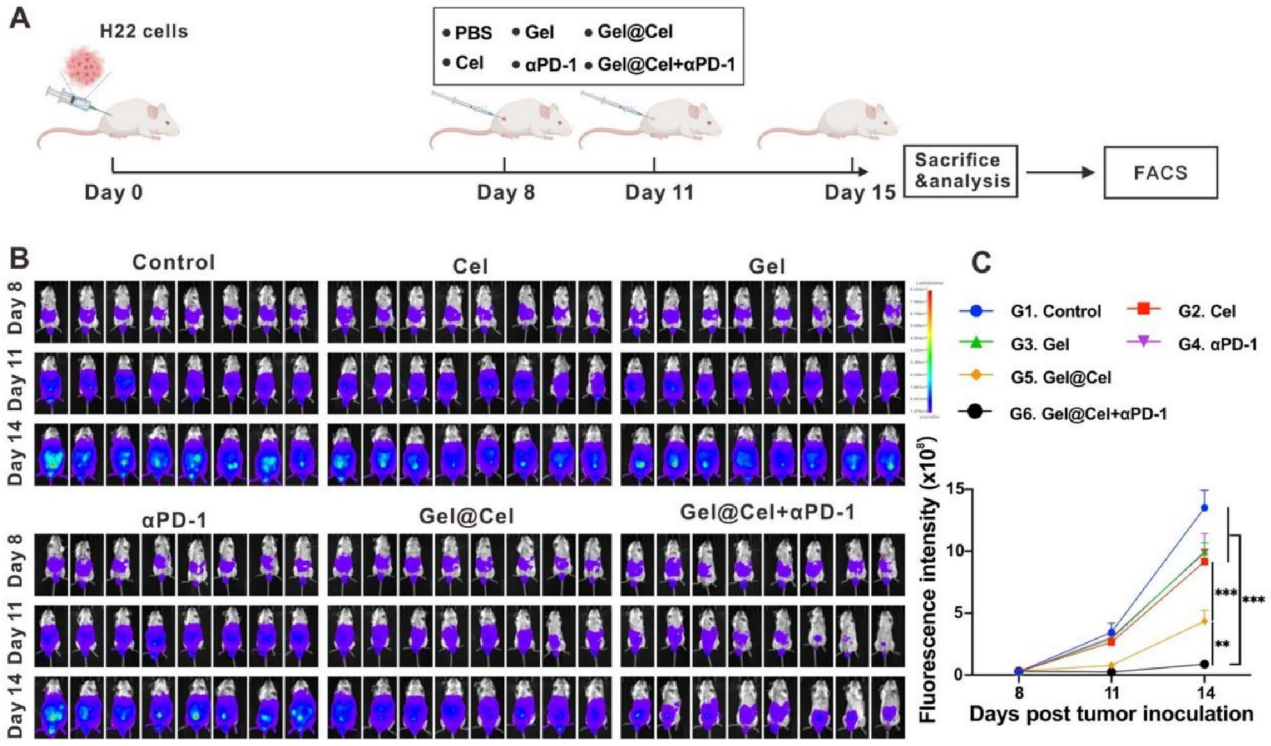

Fig. 5 Therapeutic effects of different treatments in hepatoma ascites model. **(A)** Schematic illustration of various treatment modalities (PBS, Cel, Gel, αPD-1, Gel@Cel, Gel@Cel + αPD-1) based on a H22-luc hepatoma ascites mice model. **(B)**In vivo bioluminescence images of H22-luc hepatoma ascites mice after various treatments ($n = 8$). **(C)** Quantitative analysis of the tumor bioluminescence intensity in H22-luc hepatoma ascites mice under different treatment conditions ($n = 8$). Data represent means ± S.E.M. $^{*}p < 0.05$, $^{**}p < 0.01$, and $^{***}p < 0.001$

tumor growth. Compared with Gel@Cel monotherapy, Gel@Cel + αPD-1 was more effective in reducing tumor burden (Fig. 5B-C). These results suggested that combining the αPD-1 with Gel@Cel further amplified the antitumor effect. Additionally, despite the administration of Cel in both the free Cel and Gel@Cel groups at identical doses, the Gel@Cel group exhibited a notable delay in tumor growth. This suggested that the improved release profile and enhanced therapeutic effect observed in the Gel@Cel group may be attributed to the utilization of EHG delivery systems.

In addition, the hematoxylin-eosin (H&E) staining images of normal tissues treated with different therapeutic modalities revealed no evidence of systemic adverse effects on these normal organ systems, including the heart, liver, spleen, lung, and kidney (Figure S17). Subsequently, compared with the PBS group, no significant changes in body weight were observed in mice undergoing different treatments in malignant ascites models (Figure S18). Collectively, these results indicated that our constructed EHG delivery systems demonstrated secure properties and therefore implied the biocompatibility of the EHG systems in vivo.

Evaluation of immune activation effect in vivo

Tumor-associated antigens are released from dying tumor cells undergoing ICD, following phagocytosis by antigen-presenting cells (APCs) such as DCs, and presented to T lymphocytes [23]. The gating strategy used to detect DC activation was shown in Fig. 6A. As illustrated in Fig. 6B, when compared with PBS treatment, Cel monotherapy, Gel@Cel and Gel@Cel + αPD-1 treatments increased the infiltration of activated DCs (dead dye^{-}CD45^{+}CD11c^{+}CD86^{+}), while αPD-1 monotherapy had no significant difference. Notably, the percentage of activated DCs in Gel@Cel + αPD-1 group increased by 7.0-fold and 1.3-fold, in contrast to PBS or Gel@Cel group respectively. In addition, the DC activation induced by Gel@Cel was observed to be 2-fold increase compared with free Cel, suggesting that the EHG systems employed as drug carriers had the capacity to enhance DC activation, which may be attributed to the slow-release property inherent to the EHG system. These results revealed that Gel@Cel has emerged as an effective approach for DC activation in vivo.

To evaluate the infiltration of T lymphocytes in the TME, FCM analysis revealed that the CD4^{+} T cell (dead dye^{-}CD45^{+}CD4^{+}) proportion in the PBS group was only approximately 1.3%, meanwhile the proportion of CD4^{+} T cells was up to 8.7% in the Gel@Cel + αPD-1 group,

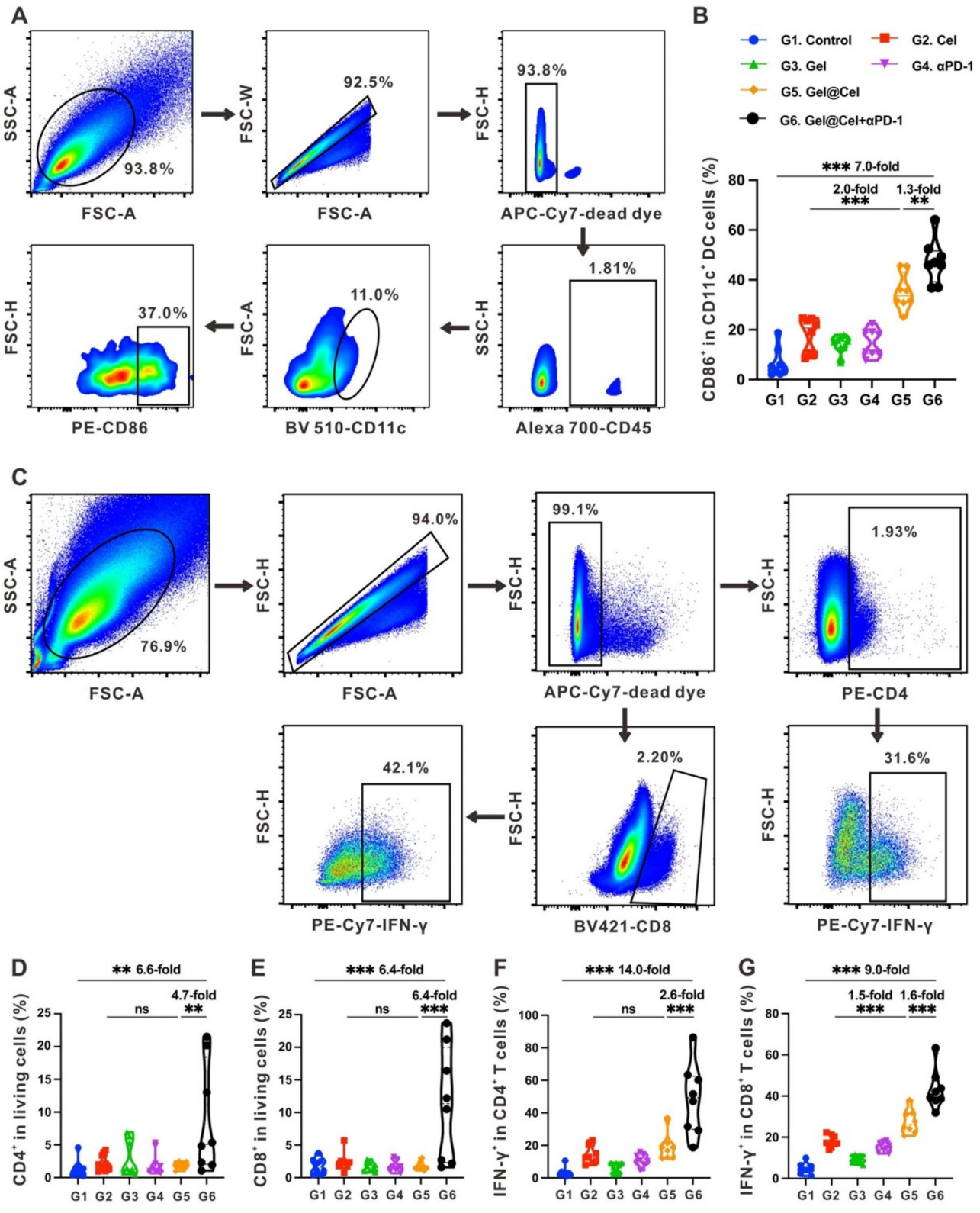

Fig. 6 Immune Activation Effect of Gel@Cel + αPD-1 in vivo. **(A)** Flow cytometry gating strategy and **(B)** quantitation of the activated DC populations in the tumors after various treatments ($n = 8$). (**C**) Gating strategy for detecting $CD4^+$ T cells, $CD8^+$ T cells, Th1 cells and CTLs by flow cytometry. (**D-G**) Relative infiltration of $CD4^+$ T cells (**D**), $CD8^+$ T cells (**E**), Th1 cells (**F**), and CTLs (**G**) in the tumors under different treatments ($n = 8$). Data represent means ± S.E.M. ns: not significant, $^*p < 0.05$, $^{**}p < 0.01$, and $^{***}p < 0.001$

increasing 6.6-fold (Fig. 6C and D). Compared with Gel@Cel, the infiltration of $CD4^+$ T cells increased by 4.7-fold in Gel@Cel + αPD-1 group. As shown in Fig. 6C and E, Gel@Cel + αPD-1 was the most therapeutic strategy that increased the proportion of $CD8^+$ T cells (dead $dye^-CD45^+CD8^+$), a 6.4-fold increase compared to PBS or Gel@Cel treatment. These results indicated that Gel@Cel + αPD-1 had the ability of potentiating therapeutic effect to relieve immunosuppression. In addition, the proportion of helper T lymphocyte 1 cells (Th1, dead $dye^-CD45^+CD4^+IFN\text{-}\gamma^+$) in the Gel@Cel + αPD-1 was elevated 14.0-fold and 2.6-fold in comparison with PBS and Gel@Cel treated tumors, respectively (Fig. 6C and F). As presented in Fig. 6C and G, the percentage of cytotoxic T lymphocytes (CTLs, dead $dye^-CD45^+CD8^+IFN\text{-}\gamma^+$) in the Gel@Cel + αPD-1 treatment was increased by 9.0-fold and 1.6-fold, compared with PBS and Gel@Cel treatment, respectively. Moreover, the infiltration of CTLs in the TME was significantly increased by 1.5-fold in the Gel@Cel group compared to the free Cel group. Generally, the afore-mentioned findings corroborated the substantial therapeutic benefits associated with the delivery of Cel via EHG in conjunction with αPD-1 for the purpose of facilitating T cell infiltration.

Discussion and conclusion

Drug delivery systems with the properties of excellent plasticity, high drug-loading efficacy, and controlled release has presented advantages for cancer immunotherapy [24–28]. Although previous research has shown that Cel as a promising Chinese herb exhibited effective antitumor efficacy against multiple tumors, its hydrophobicity, low bioavailability, and its narrow therapeutic window limited its clinical applications [12, 13, 29–31]. In comparison to conventional drug delivery systems, gel possesses satisfactory stability and bioavailability and provides aqueous environment to drugs of antitumor therapy which favors their dissolution [32–35]. Our EHG drug delivery system comprises water droplets dispersed in an oil phase, wherein the oil phase is based on clinically used iodinated oils, which have been demonstrated to be biocompatible and facilitate clinical applications. Furthermore, the EHG system permitted the controlled and gradual release of Cel in the presence of lipase by adjusting the proportion of oil. When the castor oil concentration in the oil phase reached 20 vol%, the EHG system demonstrated sustained stability, and Cel could be continuously released in response to lipase stimulation over the course of 20 days, resulting in an extended and sustained antitumor immune effect. However, in order to further enhance the clinical application of the EHG drug delivery system, future research should focus on the development of more effective biocompatibility cross-linkers. In addition, further optimization of EHG systems to make them cost-effective and reliable preparation would represent a valuable avenue of enquiry.

Malignant ascites is a major clinical challenge in the treatment of advanced hepatocellular carcinoma. Currently, conventional chemotherapy drugs (e.g., cisplatin) and anti-angiogenic drugs (e.g., bevacizumab) are commonly used to control the progress of ascites, which can temporarily relieve symptoms but is prone to recurrence [36, 37]. Clinical insensitivity to ICB therapy in patients with ascites has been reported to be mainly due to the prevalent immunosuppressive microenvironment [38, 39]. Despite the construction of multiple drug delivery systems to treat malignant ascites, the efficacy of the drugs remains limited to a short period, and repeated administration is often necessary [40]. Intraperitoneal administration of Gel@Cel to the TME of malignant ascites resulted in a gradual and controlled release of the drug due to lipase-mediated hydrolysis. In vitro and in vivo studies demonstrated that Gel@Cel inhibited tumor cell proliferation and promoted tumor cell apoptosis, while also stimulating the release of ICD signals through the activation of the AKT and MAPK pathways, thereby triggering the maturation and activation of DCs, which in turn leaded to the increased infiltration of effector T lymphocytes. Generally, Gel@Cel ameliorated the immunosuppressive TME of low-immunogenic tumors by stimulating the ICD effect. In addition, Cel, like most ICD inducers, upregulated PD-L1 expression in tumor cells [41, 42]. Hence, αPD-1 blocked the elevated PD-L1 expression in tumor cells caused by Cel, thereby achieving amplified antitumor effects in low-immunogenic tumors.

In summary, we have developed a controlled release and excellent biocompatible EHG drug delivery system loading Cel combined with αPD-1 to induce amplificatory antitumor immunity for low immunogenicity tumors. Cel effectively suppressed tumor cell proliferation while inducing the generation of ICD through the activation of the AKT and MAPK pathways, and αPD-1 blocked the elevated PD-L1 expression in tumor cells caused by Cel. Therefore, the combination of Gel@Cel and αPD-1 represents a promising approach for the treatment of tumors with low immunogenicity, offering the potential to enhance the efficacy of anticancer immunotherapy. Furthermore, further consideration could focus on optimization of our designed delivery system to enable batch preparation for clinical applications while ensuring its safety and efficacy.

Supplementary Information

The online version contains supplementary material available at https://doi.org/10.1186/s12951-025-03154-y.

Supplementary Material 1

Acknowledgements
None.

Author contributions
Yu Liu, Jia Zhang, Chunyu Lai, and Wenjun Wang made equal contributions to this work. Yu Liu and Jia Zhang focused on writing the original draft, investigation, and formal analysis. Chunyu Lai and Wenjun Wang were mainly responsible for data curation, as well as reviewing and editing the draft. Yangyue Huang contributed to the validation and review of the manuscript. Xuanwen Bao, Haimeng Yan, Xuqi Sun, and Qiqi Liu provided key support in funding acquisition. Dong Chen, Xiaomeng Dai, Xinyu Qian, and Peng Zhao played major roles in project administration and supervision, as well as coordinated resources. All authors have read and approved the final manuscript.

Funding
This research was financially supported by the National Natural Science Foundation of China (Grant No. 82473336, 82074208, 82101830, 82202875, 82200216, and 82303850), the Zhejiang Natural Science Foundation (Grant No. LY23H160013, LQ23H160029, LQ22H080001, and LQ24H160017), the Research and Development Program of Zhejiang Province (2025C02073) and the Open Research Fund of Hubei Key Laboratory of Precision Radiation Oncology (jzfs015).

Data availability
No datasets were generated or analysed during the current study.

Declarations

Ethics approval and consent to participate
All experimental protocols were approved by the Animal Experimental Ethical Inspection of the Institutional Animal Care and Use Committee and Zhejiang of Laboratory Animals with the approval number ZJCLA-IACUC-20010637.

Competing interests
The authors declare no competing interests.

Received: 29 September 2024 / Accepted: 22 January 2025
Published online: 06 March 2025

References

1. Wang H, Mooney DJ. Biomaterial-assisted targeted modulation of immune cells in cancer treatment. Nat Mater. 2018;17(9):761–72.
2. He X, Xu C. Immune checkpoint signaling and cancer immunotherapy. Cell Res. 2020;30(8):660–9.
3. Cheng AL, Hsu C, Chan SL, Choo SP, Kudo M. Challenges of combination therapy with immune checkpoint inhibitors for hepatocellular carcinoma. J Hepatol. 2020;72(2):307–19.
4. Dai X, Guo Y, Hu Y, Bao X, Zhu X, Fu Q, et al. Immunotherapy for targeting cancer stem cells in hepatocellular carcinoma. Theranostics. 2021;11(7):3489–501.
5. Kraehenbuehl L, Weng CH, Eghbali S, Wolchok JD, Merghoub T. Enhancing immunotherapy in cancer by targeting emerging immunomodulatory pathways. Nat Rev Clin Oncol. 2022;19(1):37–50.
6. Bear AS, Vonderheide RH, O'Hara MH. Challenges and opportunities for Pancreatic Cancer Immunotherapy. Cancer Cell. 2020;38(6):788–802.
7. Duan X, Chan C, Lin W. Nanoparticle-mediated immunogenic cell death enables and potentiates Cancer Immunotherapy. Angew Chem Int Ed Engl. 2019;58(3):670–80.
8. Chen X, Zhao Y, Luo W, Chen S, Lin F, Zhang X, et al. Celastrol induces ROS-mediated apoptosis via directly targeting peroxiredoxin-2 in gastric cancer cells. Theranostics. 2020;10(22):10290–308.
9. Geng Y, Xiang J, Shao S, Tang J, Shen Y. Mitochondria-targeted polymer-celastrol conjugate with enhanced anticancer efficacy. J Control Release. 2022;342:122–33.
10. Liu X, Zhao P, Wang X, Wang L, Zhu Y, Song Y, et al. Celastrol mediates autophagy and apoptosis via the ROS/JNK and Akt/mTOR signaling pathways in glioma cells. J Exp Clin Cancer Res. 2019;38(1):184.
11. Xu H, Zhao H, Ding C, Jiang D, Zhao Z, Li Y, et al. Celastrol suppresses colorectal cancer via covalent targeting peroxiredoxin 1. Signal Transduct Target Ther. 2023;8(1):51.
12. Lu S, Li Y, Yu Y. Glutathione-scavenging Celastrol-Cu nanoparticles induce self-amplified cuproptosis for Augmented Cancer Immunotherapy. Adv Mater. 2024;36(35):e2404971.
13. Wang F, Lai W, Xie D, Zhou M, Wang J, Xu R et al. Nanoparticle-mediated celastrol ER targeting delivery amplify immunogenic cell death in melanoma. J Adv Res. 2024.
14. Wang J, Zhang Z, Zhuo Y, Zhang Z, Chen R, Liang L, et al. Endoplasmic reticulum-targeted delivery of celastrol and PD-L1 siRNA for reinforcing immunogenic cell death and potentiating cancer immunotherapy. Acta Pharm Sin B. 2024;14(8):3643–60.
15. Wu L, Pi W, Huang X, Yang L, Zhang X, Lu J, et al. Orchestrated metal-coordinated carrier-free celastrol hydrogel intensifies T cell activation and regulates response to immune checkpoint blockade for synergistic chemo-immunotherapy. Biomaterials. 2025;312:122723.
16. Zhang X, Xu X, Wang X, Lin Y, Zheng Y, Xu W, et al. Hepatoma-targeting and reactive oxygen species-responsive chitosan-based polymeric micelles for delivery of celastrol. Carbohydr Polym. 2023;303:120439.
17. Kong L, Chen R, Wang X, Zhao CX, Chen Q, Hai M, et al. Controlled co-precipitation of biocompatible colorant-loaded nanoparticles by microfluidics for natural color drinks. Lab Chip. 2019;19(12):2089–95.
18. Sun Z, Yang C, Wang F, Wu B, Shao B, Li Z, et al. Biocompatible and pH-Responsive Colloidal surfactants with tunable shape for controlled interfacial curvature. Angew Chem Int Ed Engl. 2020;59(24):9365–9.
19. Qiu N, Liu Y, Liu Q, Chen Y, Shen L, Hu M, et al. Celastrol nanoemulsion induces immunogenicity and downregulates PD-L1 to boost abscopal effect in melanoma therapy. Biomaterials. 2021;269:120604.
20. Zhao Q, Liang G, Guo B, Wang W, Yang C, Chen D, et al. Polyphotosensitizer-based nanoparticles with Michael Addition Acceptors inhibiting GST activity and Cisplatin Deactivation for Enhanced Chemotherapy and photodynamic immunotherapy. Adv Sci (Weinh). 2023;10(13):e2300175.
21. Tan X, Wang C, Zhou H, Zhang S, Liu X, Yang X, et al. Bioactive fatty acid analog-derived hybrid nanoparticles confer antibody-independent chemo-immunotherapy against carcinoma. J Nanobiotechnol. 2023;21(1):183.
22. Liu X, Feng Y, Xu J, Shi Y, Yang J, Zhang R, et al. Combination of MAPK inhibition with photothermal therapy synergistically augments the anti-tumor efficacy of immune checkpoint blockade. J Control Release. 2021;332:194–209.
23. Brown MC, Holl EK, Boczkowski D, Dobrikova E, Mosaheb M, Chandramohan V, et al. Cancer immunotherapy with recombinant poliovirus induces IFN-dominant activation of dendritic cells and tumor antigen-specific CTLs. Sci Transl Med. 2017;9(408):eaan4220.
24. Jin Y, Huang Y, Ren H, Huang H, Lai C, Wang W, et al. Nano-enhanced immunotherapy: targeting the immunosuppressive tumor microenvironment. Biomaterials. 2024;305:122463.
25. Ju Y, Liao H, Richardson JJ, Guo J, Caruso F. Nanostructured particles assembled from natural building blocks for advanced therapies. Chem Soc Rev. 2022;51(11):4287–336.
26. Vincent MP, Navidzadeh JO, Bobbala S, Scott EA. Leveraging self-assembled nanobiomaterials for improved cancer immunotherapy. Cancer Cell. 2022;40(3):255–76.
27. Yang J, He Y, Zhang M, Liang C, Li T, Ji T, et al. Programmed initiation and enhancement of cGAS/STING pathway for tumour immunotherapy via tailor-designed ZnFe(2)O(4)-based nanosystem. Explor (Beijing). 2023;3(6):20230061.
28. Feng B, Lu X, Zhang G, Zhao L, Mei D. STING agonist delivery by lipid calcium phosphate nanoparticles enhances immune activation for neuroblastoma. Acta Materia Med. 2023;2(2):216–27.
29. Li H, Li Y, Zhang L, Wang N, Lu D, Tang D, et al. Prodrug-inspired adenosine triphosphate-activatable celastrol-Fe(III) chelate for cancer therapy. Sci Adv. 2024;10(28):eadn0960.
30. Lim HY, Ong PS, Wang L, Goel A, Ding L, Li-Ann Wong A, et al. Celastrol in cancer therapy: recent developments, challenges and prospects. Cancer Lett. 2021;521:252–67.
31. Niu B, Wu Y, Zhou M, Lin R, Ge P, Chen X, et al. Precise delivery of celastrol by PEGylated aptamer dendrimer nanoconjugates for enormous therapeutic effect via superior intratumor penetration over antibody counterparts. Cancer Lett. 2023;579:216461.
32. Chen Q, Wang C, Zhang X, Chen G, Hu Q, Li H, et al. In situ sprayed bioresponsive immunotherapeutic gel for post-surgical cancer treatment. Nat Nanotechnol. 2019;14(1):89–97.

33. Dai X, Zhang J, Bao X, Guo Y, Jin Y, Yang C, et al. Induction of Tumor ferroptosis-dependent immunity via an Injectable Attractive Pickering Emulsion Gel. Adv Mater. 2023;35(35):e2303542.
34. Yu S, Wang C, Yu J, Wang J, Lu Y, Zhang Y, et al. Injectable Bioresponsive Gel Depot for enhanced Immune Checkpoint Blockade. Adv Mater. 2018;30(28):e1801527.
35. Chen Z, Wu H, Wang Y, Rao Y, Yan J, Ran B, et al. Enhancing melanoma therapy by modulating the immunosuppressive microenvironment with an MMP-2 sensitive and nHA/GNE co-encapsulated hydrogel. Acta Biomater. 2024;188:79–92.
36. Gupta A, Sedhom R, Beg MS. Ascites, or Fluid in the Belly, in patients with Cancer. JAMA Oncol. 2020;6(2):308.
37. Wang Y, Sun Y, Li X, Yu X, Zhang K, Liu J, et al. Progress in the treatment of malignant ascites. Crit Rev Oncol Hematol. 2024;194:104237.
38. Chia DKA, Gwee YX, Sundar R. Resistance to systemic immune checkpoint inhibition in the peritoneal niche. J Immunother Cancer. 2022;10(6):e004749.
39. Fuca G, Cohen R, Lonardi S, Shitara K, Elez ME, Fakih M, et al. Ascites and resistance to immune checkpoint inhibition in dMMR/MSI-H metastatic colorectal and gastric cancers. J Immunother Cancer. 2022;10(2):e004001.
40. Huang A, Guo F, Yu Z, Liu P, Dong S, Zhang Y, et al. Engineered apoptosis-bioinspired nanoparticles initiate Immune Cascade for Cancer Immunotherapy of Malignant ascites. ACS Appl Mater Interfaces. 2023;15(8):10371–82.
41. Liu P, Zhao L, Pol J, Levesque S, Petrazzuolo A, Pfirschke C, et al. Crizotinib-induced immunogenic cell death in non-small cell lung cancer. Nat Commun. 2019;10(1):1486.
42. Li L, Wang J, Radford DC, Kopecek J, Yang J. Combination treatment with immunogenic and anti-PD-L1 polymer-drug conjugates of advanced tumors in a transgenic MMTV-PyMT mouse model of breast cancer. J Control Release. 2021;332:652–9.

Publisher's note